



# Enabling adenosine signaling to promote aged fracture healing



Hunter Newman<sup>1,2,3</sup>, Yu-Ru V. Shih<sup>2</sup>, Jiaul Hoque<sup>2</sup>, Yuze Zeng<sup>1,2</sup>, Naveen R. Natesh<sup>2,3</sup>, Gavin Gonzales<sup>2,3</sup>, Wendi Guo<sup>2,4</sup>, Vijitha Puvindran<sup>2</sup>, Colleen Wu<sup>2,4,5</sup>, Benjamin A. Alman<sup>2,4,5</sup> & Shyni Varghese<sup>1,2,3</sup> ✉

Bone fractures and related complications are a significant concern for older adults, particularly with the growing aging population. Therapeutic interventions that promote bone tissue regeneration are attractive for geriatric fracture repair. Extracellular adenosine plays a key role in bone homeostasis and regeneration. Herein, we examined the changes in extracellular adenosine with aging and the potential of local delivery of adenosine to promote fracture healing using aged mice. Extracellular adenosine level was found to be significantly lower in aged bone tissue compared to young mice. Concomitantly, the ecto-5'-nucleotidase CD73 expression was also lower in aged bone. Local delivery of adenosine using injectable, in situ curing microgel delivery units yielded a pro-regenerative environment and promoted fracture healing in aged mice. This study offers new insights into age-related physiological changes in adenosine levels and demonstrates the therapeutic potential of adenosine supplementation to circumvent the compromised healing of geriatric fractures.

Aging leads to progressive dysfunction of most tissues and organs, contributing to impaired tissue repair. Although there is limited clinical data directly demonstrating the sole influence of age on fracture healing outcome due to the comorbidities often present in the elderly, the impact of impaired fracture healing in elderly is a significant clinical problem<sup>1–3</sup>. Due to dysregulated inflammation, altered microenvironment including stem cell/progenitor function, pre-existing co-morbidities, and greater perioperative complications, elderly patients are often unable to return to their pre-fracture level of activity<sup>3–5</sup>. Furthermore, the elderly population suffers from higher rates of complications during fracture healing that result in increased morbidity and mortality<sup>6,7</sup>. With the increase in aged population, bone injuries with delayed healing pose a tremendous burden to the healthcare system with an estimated cost of over \$25 billion in the US alone<sup>8</sup>. Fragility fractures, or fractures due to low-level trauma, are frequent in the elderly and significantly increase hospitalization, disability, and mortality<sup>9</sup>. In the United States, 3 million fragility fractures occur annually, with almost 30% of patients experiencing mortality within 12 months following injury<sup>10</sup>. Due to the immense hardship posed by the geriatric fractures, novel therapeutic interventions to improve bone healing are of paramount importance.

The clinical management of bone injuries typically involves surgery, stabilization, administration of analgesics, and physical rehabilitation<sup>11–13</sup>. Fractures that suffer from delayed healing and nonunions typically

require repeated surgical interventions<sup>14–16</sup>. Therefore, there is a great need for new therapeutic strategies and pharmacological agents to improve fracture healing and avoid multiple surgical interventions, especially in patients with compromised or delayed healing. Fracture repair studies involving aged animals suggest that the reduction of healing results from a combination of factors such as altered vascularization and/or altered functions of both osteoprogenitor and immune cells<sup>17–19</sup>. Therapeutic interventions involving osteoanabolic molecules that promote bone tissue regeneration are attractive options to improve tissue repair and prevent delayed healing or nonunion<sup>20,21</sup>. Various osteoanabolic and angiogenic molecules have been studied in pre-clinical models to accelerate bone healing or prevent delayed healing and nonunions with varying outcomes<sup>22–26</sup>.

We and others have demonstrated the beneficial role of adenosine in bone tissue homeostasis and regeneration<sup>27–33</sup>. Adenosine is a naturally occurring nucleoside that functions through G-protein-coupled adenosine receptors — A1 receptor (ADORA1), A2A receptor (ADORA2A), A2B receptor (ADORA2B), and A3 receptor (ADORA3)<sup>34–36</sup>. The vital effect of adenosine signaling has been demonstrated in bone repair, as knocking down ADORA2A or ADORA2B in mice has resulted in impaired bone healing<sup>28,37,38</sup>. Additionally, the ectonucleotidase CD73 is a key component involved in adenosine production and is part of both classical and alternative pathways<sup>39</sup>. Altered CD73 expression is implicated in bone diseases

<sup>1</sup>Department of Mechanical Engineering and Materials Science, Duke University, Durham, NC, 27710, USA. <sup>2</sup>Department of Orthopaedic Surgery, Duke University School of Medicine, Durham, NC, 27710, USA. <sup>3</sup>Department of Biomedical Engineering, Duke University, Durham, NC, 27710, USA. <sup>4</sup>Department of Pharmacology and Cancer Biology, Duke University, Durham, NC, 27710, USA. <sup>5</sup>Department of Cell Biology, Duke University, Durham, NC, 27710, USA.

✉ e-mail: [shyni.varghese@duke.edu](mailto:shyni.varghese@duke.edu)

including osteoporosis and impaired bone healing<sup>37,40</sup>. Previously, we have identified dysregulation of ectonucleotidase-mediated extracellular adenosine in osteoporotic bone<sup>41</sup>.

In this study, we examined the changes in extracellular adenosine in bone tissue with aging. Furthermore, we formulated an in situ curing microgel delivery system containing adenosine to unravel whether local delivery of exogenous adenosine could promote fracture healing in aged mice. Our results showed a significant reduction in extracellular adenosine in the bone tissue of aged animals. Concomitant with the extracellular adenosine level, the expression level of the ecto-5'-nucleotidase CD73 was found to be significantly lowered in aged animals. Local delivery of adenosine showed enhanced fracture healing, which was found to correlate with the presence of a more pro-regenerative environment within the early callus through the modulation of immune cell signaling, as identified via scRNA sequencing.

## Results

### Decreased levels of extracellular adenosine in aged bone tissue

To examine whether there is an age-related change in the levels of extracellular adenosine, we quantified and compared the concentration of endogenous adenosine in native whole bone and marrow tissue between young (3-month-old) and aged (20-month-old) mice. The quantification showed significantly reduced levels of extracellular adenosine in aged mice compared to the young (Fig. 1a). The ecto-enzymatic cascade of CD73 (ecto-5'-nucleotidase) works in tandem with CD39 (ectonucleoside triphosphate diphosphohydrolase-1) to generate extracellular adenosine from ATP, which in turn activates adenosine receptors in a concentration and context dependent manner<sup>42</sup>. Given the key role played by CD73 in adenosine generation, we next examined the changes of CD73 expression in bone and marrow tissue between young and aged mice. Gene expression analyses showed significantly lower *Cd73* expression in aged mice bone tissue compared to young mice (Fig. 1b). Consistent with the gene expression, there were significantly less CD73<sup>+</sup> cells in the bone and bone marrow of aged mice as evident by the immunofluorescence staining and flow

cytometric analysis (Fig. 1c, d). We also examined the gene expression levels of receptors and enzymes involved in the adenosine signaling pathway, including the adenosine receptors and adenosine deaminase (ADA). No significant changes in gene expression of *Adora1*, *Adora2a*, and *Adora2b* were observed between young and aged animals (Supplementary Fig. 1a–c). In contrast, *Adora3* was significantly lower in aged bone tissue (Supplementary Fig. 1d). No age dependent significant change in *ADA* expression was detected in the gene expression analysis (Supplementary Fig. 1e). Previously, we have shown the key role played by ADORA2B in adenosine mediated osteogenic differentiation of bone marrow derived progenitor cells (MSCs) while inhibiting their adipogenesis<sup>31,32</sup>. Based on these results, we also examined the *Adora2b* gene expression in MSC populations among the aged and young mice. Notably, bone marrow-derived MSCs demonstrated significantly lower *Adora2b* expression in aged mice compared to the young (Fig. 1e).

### Local delivery of adenosine to promote aged fracture healing

Having identified the changes in extracellular adenosine levels in aged bone, we next examined the potential of local delivery of adenosine to enhance fracture healing in aged mice by using an injectable biomaterial system containing in situ curing microgels loaded with adenosine.

### Design, synthesis, and characterization of injectable, in situ curing adenosine delivery system.

The in situ curing delivery system consisted of hyaluronic acid (HA) microgels loaded with adenosine and functionalized with ureidopyrimidinone (UPy) molecules, which facilitated annealing of the microgels and network formation *via* hydrogen bonding (Fig. 2a–d). Details of the synthesis and characterization are provided in the Methods and Supporting Information (Fig. 2a–d; Supplementary Fig. 2–5). The average size of the microgels was found to be  $\sim 159 \pm 10 \mu\text{m}$  (Fig. 2e). The microgels remained stable for 28 days (maximum experimental time observed) in both water and growth media containing serum as no significant change in diameter was observed (Supplementary Fig. 6). UV-visible absorption spectroscopy analysis indicated that the

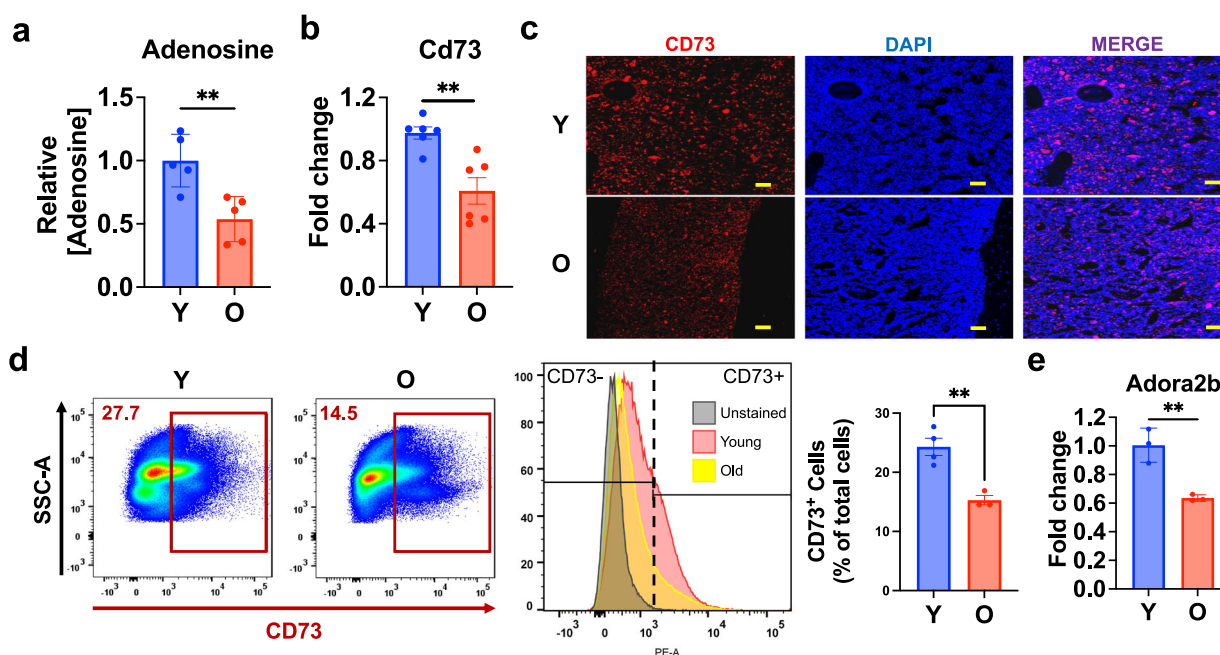


**Fig. 1 | Perturbation of extracellular adenosine in the aged bone marrow.** The bone of young (Y, 3 mo.) and old (O, 20 mo.) mice were harvested and compared for their extracellular adenosine levels and cellular expression of CD73. **a** Extracellular adenosine levels from bone marrow (mean  $\pm$  SEM,  $n = 5$  mice per group). **b** Gene expression of *Cd73* in bone and marrow cells (mean  $\pm$  SEM,  $n = 6$  mice per group). **c** Immunofluorescence staining of CD73. DAPI stains the nucleus blue. Scale bar,

100  $\mu\text{m}$ . **d** Flow cytometric analyses of CD73 expression in bone marrow cells (mean  $\pm$  SEM,  $n = 3-4$  mice per group). **e** Gene expression of *Adora2b* in bone marrow-derived mesenchymal stromal cells (MSCs; mean  $\pm$  SEM,  $n = 3$  and 2 mice were pooled per group). Statistical analyses were performed by two-tailed unpaired *t* test. \*\* $P < 0.01$ .

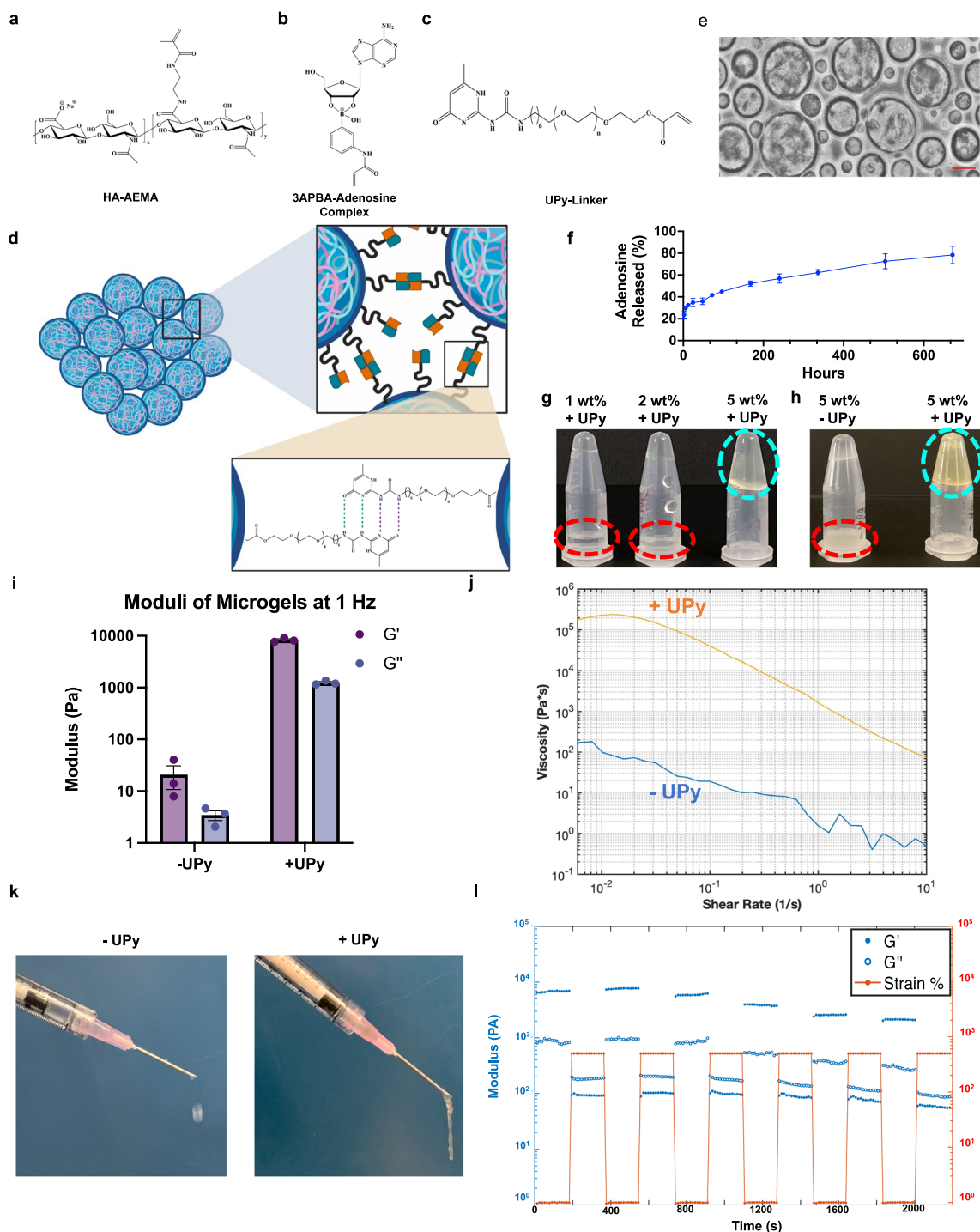


**Fig. 2 | Adenosine-containing microgels.** Chemical structures of the microgel components: (a) HA-AEMA, (b) 3-APBA-adenosine, and (c) the UPy linker. d Schematic depicting microgel scaffold formation due to hydrogen bonding between the UPy moieties. e Representative image of the adenosine-containing microgels hydrated in distilled H<sub>2</sub>O (scale bar: 100 μm). f Cumulative release of adenosine from the microgels in PBS buffer of pH 7.4 as a function of time. g Vial inversion test comparing 5 wt%, 2 wt%, and 1 wt% microgel scaffolds with UPy.

h Vial inversion test comparing 5 wt% microgel scaffolds with or without UPy. i Storage moduli of microgel scaffolds with or without UPy at a frequency of 1 Hz and 1% strain (mean ± SEM). j Viscosity as a function of shear rate comparing 5 wt% microgel scaffolds with or without UPy. k Extrusion of microgel scaffolds with and without UPy through an 18-gauge needle. l Step-strain measurements for microgel scaffold containing UPy.

microgel contained  $\sim 453 \pm 27$  μg of adenosine per mg of the microgel. To test the adenosine release from the microgel scaffold, the release kinetics were determined at pH 7.4 over a period of 28 days. Similar to previous reports<sup>43,44</sup>, an initial burst release followed by a sustained release of adenosine was observed until 28 days, where the release began to level off (Fig. 2f).

The UPy-mediated gelation of the microgels was characterized initially by visualizing the flow behavior of the solution containing the microgels functionalized with or without UPy. The UPy-mediated gelation was investigated for different concentrations of 1, 2, and 5 wt%. The UPy-modified microgels exhibited a solid-like behavior at 5 wt% and did not flow upon vial inversion (Fig. 2g). In contrast, samples containing microgels

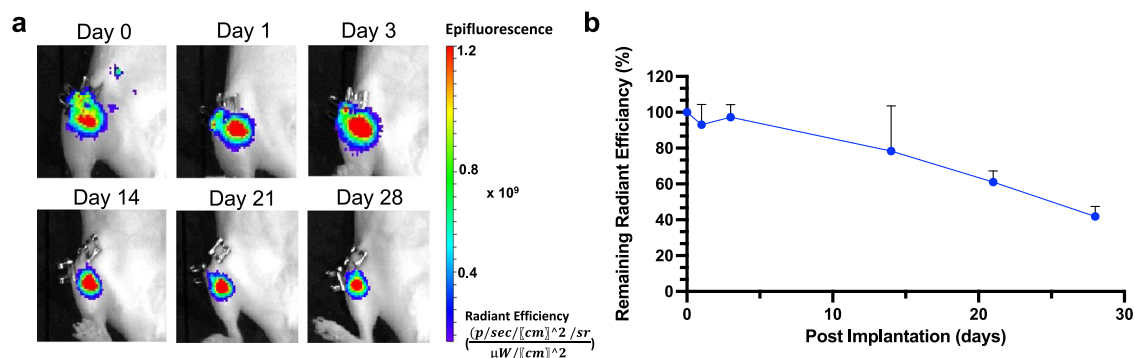


**Fig. 3 | In vivo retention of adenosine-containing in situ curing microgel system.** a Representative IVIS images of mouse fractured tibiae following injection of Cy7-conjugated adenosine-containing microgels at the fracture site as a function of time.

The fluorescence intensity is reflected using a color map on the right. b Quantification of fluorescence intensity expressed as a percentage of initial intensity. (mean + SEM,  $n = 2$ ).

without the UPy modification behaved like a liquid suspension at all concentrations, including 5 wt% (Fig. 2h). The network formation was also confirmed by rheological measurements. Frequency sweep measurements demonstrated UPy mediated gelation at 5 wt%, as a much higher storage ( $G'$ ) modulus was observed for microgels with UPy than the microgels devoid of UPy (Fig. 2i). Notably, for the UPy containing microgel, the storage ( $G'$ ) modulus was higher than the loss ( $G''$ ) modulus, which indicated crosslinking of the microgels. As expected, the UPy containing microgels showed an increase in moduli with an increase in UPy concentration (Supplementary Fig. 7). Shear rate sweep measurements of the UPy microgel system demonstrated shear thinning behavior (Fig. 2j). Consistent with the shear thinning behavior, the UPy modified microgels could easily be extruded through an 18-gauge needle (Fig. 2k).

Given the dynamic nature of hydrogen bonds, the microgel networks should be able to self-heal and regenerate the networks following rupture<sup>45</sup>. To examine the self-healing ability of the microgel network, we conducted step-strain measurements. 5 wt% microgel suspensions were subjected to altering step strains of 1% and 500% (Fig. 2l). The  $G'$  and  $G''$  values of the UPy-microgel scaffold inverted at a 500% strain, indicating disruption of the hydrogen bonds between the microgels. After the strain was removed, the microgels reorganized and generated the network with 100% storage modulus recovery.

### Adenosine delivery promotes aged fracture healing

To evaluate the ability of the adenosine-loaded injectable microgel scaffolds to repair aged bone tissues, we utilized a tibial fracture model<sup>43,44,46</sup>. The retention of the in situ curing microgels following injection was assessed by using Cy7-conjugated microgels. Longitudinal IVIS imaging for 28 days following local administration of the microgels to the tibial fracture showed their localization at the fracture site with minimal loss of radiant efficiency in the initial 3 days, followed by a gradual decrease of signal to ~42% by 28 days post-administration (Fig. 3a, b).

Stabilized tibial fractures were treated with either the control microgel scaffold lacking adenosine, or the microgel units loaded with adenosine. Treatment-dependent changes in fracture healing were analyzed at various timepoints of 7, 14, and 28 days. We also analyzed the expression of several pro-regenerative markers that are known to play an important role in fracture healing, including the angiogenesis marker VEGF, as well as PDGFA and IGF1<sup>47–49</sup>. Gene expression analyses of the callus at 7 days post-fracture showed significantly higher expressions of *Vegf* and *Pdgfa* in adenosine treated groups compared to controls (Fig. 4a, b). *Igf1* expression demonstrated an increasing trend in the adenosine-treated group compared to the control, albeit not significant (Fig. 4c). Callus gene expression analysis was also conducted at 3 days post-fracture, where the *Vegf* expression was higher in the adenosine treated group compared to the control, while *Pdgfa* and *Igf1* expressions did not show any significant changes (Supplementary Fig. 8); the *Igf1* again displayed an increasing

trend in the adenosine treated group compared to the control (Supplementary Fig. 8c).

To evaluate the healing progression of the fractures, microcomputed tomography (microCT) and histological staining (Movat's Pentachrome and Safarin-O) were used for morphological analysis of the fractured calluses. The 7-day post-fracture calluses did not demonstrate significant differences between the control and adenosine-treated groups (Fig. 4d–f). However, 14- and 28-day post-fractured calluses showed visible differences in healing with the adenosine group showing an overall improved healing compared to the control group (Fig. 4d–f). The control group exhibited a less mature and less organized callus with increased cartilaginous tissue remaining at 14 days. In contrast, the adenosine-treated group showed reduced cartilaginous tissue, new bone deposition, and better alignment of cortices with a smaller distance between them at 28 days (Supplementary Fig. 9). In addition, the adenosine-treated group displayed near-union of the cortices, along with a reduced number of cortical fragments remaining in the callus at 28 days post-fracture (Fig. 4e, f). This was complemented by microCT parameters at 28 days, which demonstrated a significantly decreased callus in the adenosine-treated group (TV). Other parameters, such as bone mineral density (BMD) and bone volume ratio (BV/TV), showed a positive trend, but no statistical significance (Supplementary Fig. 10a–c). Examination of vascularization in the fracture calluses using immunofluorescent staining showed significantly increased endomucin-positive staining in adenosine-treated group at 28 days compared to control, while the 7- and 14-day time points showed a trend of increasing staining in the adenosine-treated group (Fig. 4g; Supplementary Fig. 11).

### scRNA-Seq analysis of cells in post-fractured callus

To examine the effect of adenosine on cell populations contributing to the early pro-regenerative environment within the fracture callus, we performed scRNA-seq analysis on bone marrow cells from the callus. The bone marrow tissues were harvested 7-days post-fracture from aged animals either treated with the control microgel lacking adenosine, or the adenosine containing microgels. Our analysis focused on immune cells, as immune cell signaling is critical to the resolution of inflammation and induction of the regenerative phase of fracture healing<sup>50</sup>. Initial unbiased clustering revealed 11 cell clusters in the composite UMAP (Fig. 5a). Distinct cluster analysis revealed both the control and adenosine treated groups exhibiting all 11 cell clusters with varying cell numbers and proportions (Fig. 5a–c). For both groups, granulocytes were the most abundant cells population; however, the adenosine treated groups showed a decreased number of granulocytes compared to the control group. Moreover, adenosine treatment resulted in an increase in T cells, B cells, and progenitor cells within the callus (Fig. 5a–c).

To determine if adenosine treatment influenced overall gene expression within the callus, we examined the gene expression across all cell clusters. Some of the top genes that were significantly decreased in the adenosine treated group compared to the control group were the

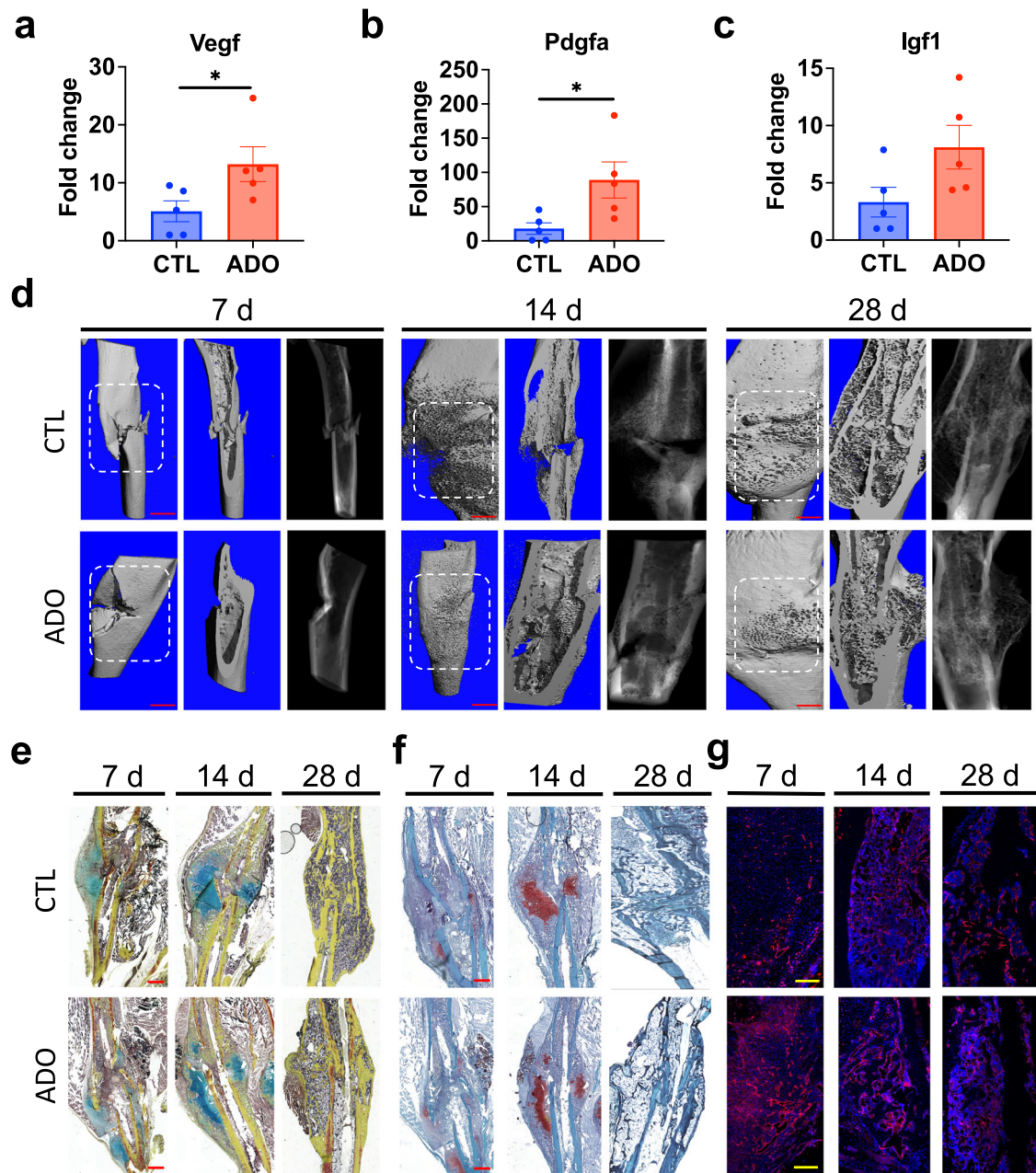


**Fig. 4 | Local delivery of adenosine promotes bone regeneration in aged mice.** The fractured tibiae of old (20 mo.) mice treated with control (microgel without adenosine) or adenosine-loaded microgels were harvested and analyzed for gene expression analyses or histology. Gene expression of (a) *Vegf*, (b) *Pdgfa*, and (c) *Igf1* at 7 days post-fracture (mean  $\pm$  SEM,  $n = 5$  mice per group). Statistical analyses were performed by two-tailed unpaired *t* test.  $*P < 0.05$ . **d** Representative 3D reconstructed images (both whole and cut views) and radiographs of the fractured tibia treated with control or adenosine-containing microgel scaffolds at 7-, 14-, or 21-days

following injury (white boxes outline the callus region) scale bar: 1 mm. Representative (e) Movat’s Pentachrome and (f) Safranin-O stained images of fractured tibiae treated with control or adenosine-containing microgel scaffolds at 7-, 14-, or 21-days following injury. scale bar: 900  $\mu$ m. **g** Representative immunofluorescence images of endomucin (red) staining demonstrating vascularization of fractured calluses treated with control or adenosine-containing microgel scaffolds at 7-, 14-, or 21-days following injury (scale bar: 200  $\mu$ m).

transcription factor CCAAT/enhancer binding protein beta (*Cebpb*), chemokine (C-X-C motif) ligand 2 (*Cxcl2*), cytokine interleukin 1 beta (*Il1b*), and thrombospondin 1 (*Thbs1*) (Fig. 5d; Supplementary Fig. 12a–d). These findings suggest a decrease in pro-inflammatory factors that are known to effectively negatively influence bone regeneration following treatment with adenosine.

As granulocytes comprised the most abundant population, we sought to explore them further for their potential transcriptomic differences using RNA velocity. RNA velocity enables determination of transcriptional dynamics within single cells, using various solvers of differential equations

(i.e. stochastic, deterministic, dynamic)<sup>51</sup>. We performed RNA velocity on the unbiased clusters of post-clustering labeled granulocytes for both the experimental groups in our scRNA-seq dataset, and observed a clear dynamical progression towards a cluster, cluster 4, enriched in the callus of the control group (Fig. 5e). Of note the cluster 4 was abundant in the control group compared to adenosine treated group. The velocity vectors appeared to change direction before returning towards the cluster 4. To understand this, we further performed differential velocity t-testing to identify genes driving the velocity vectors from cluster 3 to cluster 4, discovering *Il1b* as the highest ranked gene for cluster 3 in both adenosine and control groups.

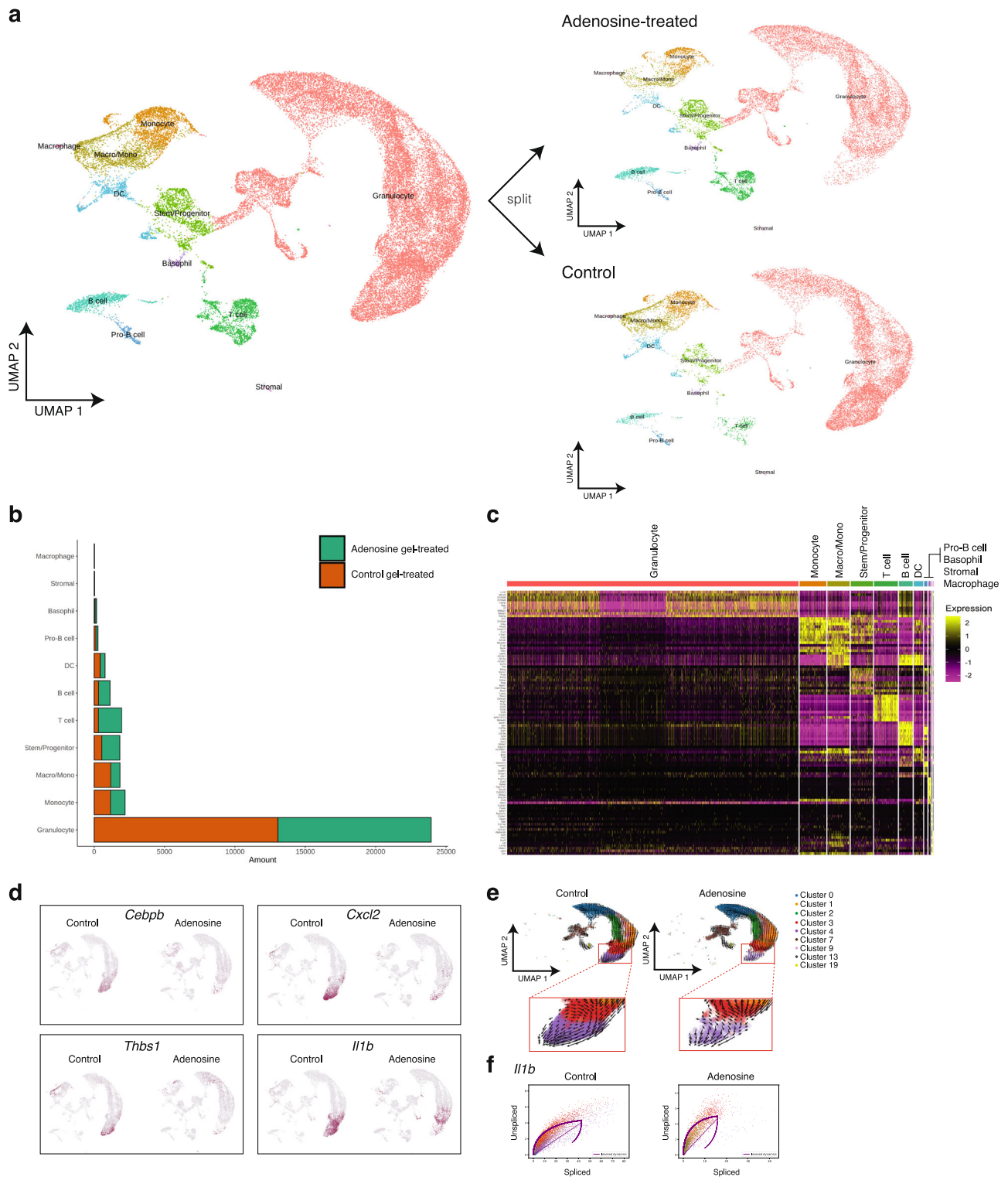


**Fig. 5 | scRNA seq of 7-day fractured callus in aged mice.** Single-cell transcriptomic analysis of fractured callus in aged mice treated with control (microgel without adenosine) or adenosine-loaded microgels. **a** Uniform manifold approximation and projection (UMAP) of complete dataset with annotated cell clusters split by experimental group. **b** Numerical abundances of each identified cell type, colored by experimental group. **c** Heatmap illustrating marker gene expression for each of the identified cell clusters in the full dataset. **d** Feature plots with gene expression of

select genes between aged mice treated with control or adenosine-containing microgel scaffolds. **e** RNA velocities of granulocyte clusters projected onto UMAP (red inset shows velocities from cluster 3 to cluster 4). **f** Scatter plot depicting abundance of spliced and unspliced reads for *Il1b* gene expression between control- and adenosine-containing microgel treated calluses (solid purple line shows inferred trajectory; dashed line shows inferred steady-state ratio).

Figure 5F depicts a phase portrait demonstrating the induction of *Il1b* gene expression through the spliced:unspliced RNA ratio, and a relative decrease in the induction of *Il1b* expression in adenosine treated groups (purple curve in Fig. 5f). Taken together, the expression dynamics of *Il1b* may be affected by adenosine treatment, thereby influencing the resultant granulocyte subtypes.

## Discussion

Aging has been shown to negatively affect the cellular and molecular processes associated with fracture repair<sup>3</sup>. Inadequate neovascularization<sup>52</sup> and decreased osteoprogenitor/stem cell function<sup>53</sup> are identified as some of the factors contributing to poor healing outcomes in the elderly<sup>3</sup>. Therefore, therapeutics that can overcome the age-related deficits in bone repair could significantly improve the fracture healing. Previously, we have shown that localization of extracellular adenosine at the fracture site promoted fracture healing in young mice via improved angiogenesis and osteoblastogenesis<sup>27</sup>. Bone degenerative diseases like osteoporosis are associated with reduced extracellular adenosine in the bone tissue<sup>41</sup>, which led us to investigate the possibility of altered adenosine signaling as a contributing factor to impaired fracture healing in aged animals.

Our results show that the extracellular adenosine and CD73 expression are substantially decreased in the aged bone tissue. The decrease in CD73 expression in conjunction with an unaltered adenosine deaminase expression, which irreversibly deaminates adenosine to inosine<sup>54</sup>, between young and aged animals indicated that the reduction of adenosine levels in aged bone tissue is associated with decreased extracellular adenosine production rather than increased adenosine catabolism. Taken together, these findings provide new insights into the physiological perturbations of adenosine signaling in aged mice that could potentially contribute to delayed fracture healing.

While gene expression analyses of adenosine receptors of the whole bone marrow showed no significant change for A1 and A2 adenosine receptors between the young and the old, significant difference in ADORA3 was observed. Although understandings of the role of ADORA3 in bone health remains minimal, studies have shown that it plays a key role in reducing inflammation via neutrophils and mast cells<sup>55–57</sup>. We speculate the *Adora3* decrease may result in deficient resolution of inflammation in aged mice, a process required for normal bone healing<sup>50,57</sup>. ADORA3 agonism has been shown to significantly decrease the release of inflammatory cytokines such as *Il1b*<sup>58–61</sup>. This is supported by our scRNA sequencing results which demonstrated a decrease in *Il1b* expression in the adenosine-treated group.

Previously, we have shown that harnessing the transient increase in endogenous adenosine following injury at the fracture site promotes bone healing in young mice<sup>44</sup>. However, since endogenous adenosine levels are significantly decreased in aged mice, sequestering the nucleoside in situ at the fracture is not a viable treatment option. Therefore, we developed a local delivery system consisting of microgels serving as both building blocks for a 3D scaffold and a drug carrier to deliver adenosine locally at the fracture site. Local delivery of adenosine will circumvent the challenges associated with the ubiquitous presence of adenosine receptors as well as the short half-life of adenosine in circulation, in which local delivery could improve its bioavailability and mitigate the off-target effects. The microgels encoded with ureidopyrimidinone (UPy) moieties, which is known to rapidly dimerize *via* quadruple hydrogen-bonding, facilitates annealing of the microgel units to form a dynamic 3D scaffold. The reversible network formation contributes to the shear thinning behavior, which in turn facilitates its injectability and ease of administration<sup>45</sup>.

The aged mice treated with adenosine showed improved fracture healing as suggested by the microCT and histochemical analyses. Concomitant with the accelerated fracture healing timeline, the early fracture calluses showed an increase in pro-regenerative growth factors and a decreased inflammatory environment. Previous studies have shown that adenosine promotes *Vegf* expression and angiogenesis through A2A receptor signaling<sup>30,62</sup>, while its effect on *Pdgfa* and *Igf1* expression remains

unknown. The increase in *Vegf* was complemented by an increase in endomucin positive staining at early time points during healing.

The adenosine treated groups showed improved healing at all time-points when compared to the controls. The healing timeline was expedited in the adenosine treated groups, as evident by the reduction in cartilage template at the mid stage of healing when compared to the controls. While this study focused on adenosine delivery to promote fracture healing in aged mice that display low levels of endogenous adenosine, our previous studies with 3-month-old young mice demonstrated that biomaterial-assisted sequestration of transiently upregulated adenosine following a fracture can enhance healing<sup>44</sup>. Hence, although the control group does not receive exogenous adenosine, it is possible that the material could sequester extracellular adenosine, if present, albeit at low levels in aged mice. This could explain some of the varied healing parameters in control group.

Animals with delayed endochondral healing have previously demonstrated to exhibit compromised healing and inferior biomechanical properties of the neo-bone<sup>63</sup>, and treatments that can accelerate endochondral ossification have been shown to attenuate impaired healing<sup>64</sup>. Together, these data indicate the possible role of adenosine in creating a pro-regenerative environment through modulation of immune cell signaling and vascularization to promote fracture healing. While the results of this study suggest that adenosine delivery promotes fracture healing, the quality and functionality of the newly formed tissue require further investigation. Specifically, the study lacks mechanical characterization of the repaired bone, which is essential to assess the structural integrity and healing quality of the tissue.

In summary, our results identified a significantly lower adenosine level in aged animals compared to their younger counterparts. The lower levels of extracellular adenosine were correlated with the significantly lower expression of CD73 in aged bone. Supplementing extracellular adenosine at the fracture site by using a biomaterial—injectable building blocks and adenosine—accelerated fracture healing in aged mice. The scRNA sequencing indicates that the local delivery of adenosine altered the immune cell signaling to induce both vascularization and osteogenesis, and thereby creating a pro-regenerative environment. This study demonstrates the therapeutic potential of using adenosine treatment to bolster the impaired healing capacity of aged fractures. While the work here demonstrates perturbations of aged adenosine signaling and the ability of adenosine delivery to generate a pro-regenerative environment to expedite aged fracture healing, further investigation is needed to unravel the specific down-stream pathways involved and the spatiotemporal changes.

## Methods

### Animal studies

All animal studies were performed with the approval of Institutional Animal Care and Use Committee (IACUC) (A151-20-07) through Duke University and in accordance with the guidelines from the National Institutes of Health (NIH). 3-month-old and 20-month-old male C57BL/6 J mice (Jackson Laboratory) were used for cell isolation and in vivo studies. Young and old mice were also used for flow cytometry analysis and the adenosine assay. The number of mice used per group are indicated in the corresponding figure legends. All euthanasia procedures were carried out in compliance with the ARRIVE 2.0 guidelines and adhered to the recommendations of the American Veterinary Medical Association (AVMA). Mice were euthanized via inhalation of isoflurane followed by a secondary physical method to confirm death. Mice were placed in an induction chamber pre-filled with 3–5% isoflurane in oxygen delivered at a flow rate of 1–2 L/min. The animals were monitored for signs of deep anesthesia, confirmed by the loss of reflexes (e.g., pedal withdrawal reflex) and absence of voluntary movement. To confirm death, mice were subjected to a secondary method of euthanasia, cervical dislocation.

### Adenosine assay

Bone marrow was collected from both femurs and tibiae. Plasma was isolated from the bone marrow flush by centrifugation at 2000 rcf for 20 min at

4 °C, and the supernatant was collected and mixed with an adenosine-buffer solution containing 0.2 mM dipyrindamole, 5 μM erythro-9-(2-hydroxy-3-nonyl)-adenine, 60 μM alpha, beta-methylene-adenosine 5'-diphosphate, and 4.2 mM ethylenediaminetetraacetic acid (EDTA). An Adenosine Assay Kit (Fluorometric; Abcam, ab211094) was used to quantify the extracellular adenosine content in the plasma. Each sample was mixed with the designated reagents consisting of Adenosine Detector, Adenosine Converter, Adenosine Developer, and Adenosine Probe in the Adenosine Assay Buffer, and the mixture was incubated in dark for 15 min. Adenosine concentration was determined based on fluorescence intensity at 535 nm (excitation)/590 nm (emission) using a microplate reader; known concentrations of adenosine were used as standards.

### Quantitative reverse transcription PCR

Ribonucleic acid (RNA) from tissues or cells were extracted with TRIzol, phase-separated with chloroform, and precipitated in isopropanol. One microgram of RNA was reverse transcribed with iScript cDNA Synthesis Kit (Bio-Rad, Hercules, CA, 1708891), according to the manufacturer's instructions<sup>65</sup>. Quantitative PCR was performed with iTaq Universal SYBR green reagent (Bio-Rad, 1725124) using denaturation at 95 °C for 30 seconds for one cycle, and amplification (denaturation + annealing/extension) at 95 °C for 5 s and 60 °C for 30 s for 40 cycles on a polymerase chain reaction cyclor (Bio-Rad, CFX96 Touch). The primer sequences are: *Cd73* (forward, GGTCC ACCCTG AAGAA GGCT; reverse, CTCTG TTCCA GGGCT TTCGG), *Ada* (forward, CGGAG AGAAC CGGA ACAC; reverse, TGGTT TCTGG CITGA TGGCT), *Adora1* (forward, CCCCC TCGTCTA TGCCCTCC; reverse, CATCG GAAGT GGTCG TTCCA), *Adora2a* (forward, GCCAG AGCAA GAGGC AGGTA T; reverse, TCCCA AAGGC TTTCT CACGG), *Adora2b* (forward, ATCTT TAGCC TCTTG GCGGT G; reverse, GACCC AGAGG ACAGC AATGA T), *Adora3* (forward, GCTGT A GACCGA TACCTG CG; reverse, GGAAAC TAGCCA GCAAAG GC), *Vegf* (forward, TGGACCCTGGCTTTACTGCT; reverse, CAATCGGACGGCAGTAGCTT),

*Pdffa* (forward, GTCCAGGTGAGGTTAGAGG; reverse, CACGGA GGAGAACAAGAC), *Igf1* (forward, CAACATCTCCCATCTCTCT GGA; reverse, TTGGGTTGGAAGACTGCTGA), *18S ribosomal RNA* (forward, ACCAG AGCGA AAGCA TTTGC CA; reverse, ATCGC CAGTC GGCAT CGTTT AT). The expression level of each target gene was normalized to both the housekeeping gene and their respective controls. The expression level was presented as fold change expressed as  $2^{-\Delta\Delta Ct}$ .

### Flow cytometry analysis

Long bones of mice were dissected and washed with PBS. The bones were pulverized, and marrow flushed with PBS. Cell debris was removed by passing through a 70 μm cell strainer. Cells were pelleted using centrifugation at 300 × g, and the supernatant was removed. The cells were then treated with Red Blood Cell Lysis Buffer (Thermo Fisher, Waltham, USA) for 5 min at 25 °C. Cells were again centrifuged and the supernatant was removed. Flow Cytometry Staining Buffer (Thermo Fisher, Waltham, USA) was then added to the cells. The cells were stained with the LIVE/DEAD Fixable Near-IR Dead Cell Stain Kit (Thermo Fisher, L10119) for 30 min at 25 °C. Cells were washed twice with PBS and incubated with CD73 primary antibody (Thermo Fisher, 12-0731-82; 1:100 dilution) at 4 °C for 30 min. Cells were then washed twice with PBS, and flow cytometry was performed on BD FACSCanto II (BD Biosciences, 338962). FlowJo software (version 10.6.1) was used to analyze the results. OneComp eBeads Compensation Beads (Thermo Fisher, 01-1111-41) and ArC Amine Reactive Compensation Beads (Thermo Fisher, A10346) were used for compensation.

### Reagents and chemicals for biomaterial synthesis

Hyaluronic acid (MW 40 kDa, HA40K) was obtained from Lifecore, USA. 2-Aminoethylmethacrylamide (2-AEMA), 24833-5) was acquired from Polysciences, USA. Sodium hydroxide (NaOH, 795429), 17-azido-3,6,9,12,15-pentaoxaheptadecan-1-amine (901155), N-hydroxysuccinimide (NHS, 130672), 2-amino-4-hydroxy-6-methylpyrimidine (UPy, A58003),

hexamethylene diisocyanate (NCO, 52649), acryloyl chloride (A24109), mineral oil (M5904), and adenosine (A4036) were obtained from MilliporeSigma, USA. 3-acrylamido phenylboronic acid (3-APBA) (A3199) and 1-ethyl-3-(3-dimethylaminopropyl) carbodiimide hydrochloride (EDC.HCl, D1601) were purchased from TCI Chemicals, USA. Triethanolamine (AC139560010) and triphenylphosphine (PPH<sub>3</sub>, 14112) were purchased from Fisher Scientific, USA. The dialysis bags (MWCO 3.5 kDa) were obtained from Repligen, USA. ABIL EM90 surfactant (420095-L-151) was obtained from Universal Preserv-A Chem INC, Germany. Hexane, acetone, ethanol, dichloromethane (DCM), and dimethyl sulfoxide (DMSO) were ACS grade and purchased from MilliporeSigma, USA. Methanol was purchased from Fisher Scientific, USA, and of ACS grade. Genesys 10S UV-VIS spectrometer was used to record UV-visible spectra. FTIR spectra were recorded using the Thermo Electron Nicolet 8700 FTIR spectrometer. NMR spectra were recorded using an FSC 400 MHz Agilent/Varian Inova spectrometer.

### Synthesis of 2-aminoethylmethacrylamide (2-AEMA)-conjugated hyaluronic acid (HA-AEMA)

HA-AEMA was prepared by conjugating 2-aminoethylmethacrylamide (2-AEMA) to hyaluronic acid (HA) through activation of the carboxylic acid. In short, HA (400 mg) was dissolved in MES buffer of pH 5.5 at a concentration of 10 mg/mL. 1-Ethyl-3-(3-dimethylaminopropyl)carbodiimide hydrochloride (EDC.HCl, 384 mg) and N-hydroxysuccinimide (NHS, 230 mg) were added to the HA solution in 15 min intervals. 2-AEMA (164 mg, 1 equivalent with respect to the carboxylic acid groups of HA) was added to the reaction mixture after 30 min and allowed to react for 24 h at 25 °C. The resulting reaction mixture was dialyzed and lyophilized to obtain HA-AEMA. The degree of AEMA conjugation, determined via <sup>1</sup>HNMR, was 17±1 (Supplementary Fig. 3).

### Synthesis of Cy7-conjugated hyaluronic acid

Cyanine 7 (Cy7) fluorescently labeled HA was created by Cy7 amine conjugation to the HA-AEMA through amide coupling reaction between the amine groups of Cy7 and the free carboxylic acid groups of HA-AEMA. 100 mg of HA-AEMA was dissolved in a 1:1 deionized water: DMSO mixture at a concentration of 5 mg/mL. To this solution, 69 mg of EDC.HCl and 41.4 mg of NHS were added at 15 min intervals. 6 mg of Cy7 dissolved in 1 mL of DMSO was added to the reaction mixture and reacted at 25 °C for 2 days. The resulting product was dialyzed against 10:1 deionized water: DMSO mixture for 24 h using a cellulose acetate dialysis bag with MWCO 3.5 kDa. This was followed by 5 days of dialysis against deionized water. The resulting HA-AEMA-Cy7 product was then lyophilized and stored at -20 °C.

### Synthesis of UPy linker

UPy linker was synthesized in a stepwise procedure. First, 17-azido-3,6,9,12,15-pentaoxaheptadecan-1-amine (1.1 g) and triethylamine (729 mg) were reacted with acryloyl chloride (487 mg) in dichloromethane at 25 °C overnight. The resulting solution was washed with 1 N HCl, saturated sodium bicarbonate, and brine solution, and dried using the rotary-evaporator to obtain N-(17-azido-3,6,9,12,15-pentaoxaheptadecyl)acrylamide, which was characterized via <sup>1</sup>HNMR (Supplementary Fig. 4). Next, N-(17-azido-3,6,9,12,15-pentaoxaheptadecyl)acrylamide (1.1 g) was dissolved in methanol and reacted with triphenylphosphine (1.1 g) overnight. The reaction mixture was dried via rotary-evaporation and dissolved in excess distilled water. The solution was washed multiple times with ethyl acetate. Finally, the water layer was freeze-dried to obtain the product, N-(17-amino-3,6,9,12,15-pentaoxaheptadecyl)acrylamide. Separately, 2-amino-4-hydroxy-6-methylpyrimidine (10 g) was dissolved and reacted in excess hexamethylene diisocyanate (107 g) at 100 °C overnight under an argon environment. The product, 1-(6-isocyanatoethyl)-3-(6-methyl-4-oxo-1,4-dihydropyrimidin-2-yl)urea, was precipitated, washed with pentane, and dried under vacuum. Finally, N-(2-(2-(2-aminoethoxy)ethoxy)ethyl)acrylamide (816 mg) and 1-(6-isocyanatoethyl)-3-(6-methyl-4-oxo-

1,4-dihydropyrimidin-2-yl)urea (410 mg) were dissolved in N,N-dimethylformamide and reacted at 55 °C for 24 h. The resulting UPy linker, N-(1-((6-methyl-4-oxo-1,4-dihydropyrimidin-2-yl)amino)-1,10-dioxo-14,17,20,23,26-penta-oxa-2,9,11-triazaoctacosan-28-yl)acrylamide, was precipitated using a 50:50 diethyl ether:acetone mixture, dried in a vacuum oven at 40 °C, and characterized *via* <sup>1</sup>HNMR (Supplementary Fig. 5).

### Synthesis of adenosine-containing microgels

The microgels were synthesized through an inverse emulsion suspension co-polymerization as described previously<sup>43</sup>. First, adenosine was conjugated to 3-(acrylamido)phenylboronic acid (3-APBA) at ~pH 11 to obtain an adenosine-PBA complex. Briefly, 3-APBA (191 mg) was dissolved in water (750 µL) by adjusting the pH to approximately 11 by using 5 N NaOH. Adenosine (267 mg) was added to the PBA solution and dissolved to obtain a clear solution. This solution was then added to 75 mg of freeze-dried HA-AEAM and allowed to dissolve. Separately, the UPy-linker (75 mg) was dissolved in water (250 µL) in presence of 5 N NaOH (at pH 10). Both the solutions were mixed and 2,4,6-trimethylbenzoylphosphinate (LAP) was added to obtain the final concentrations of HA-AEMA: 7.5 wt%; 3-APBA: 1 M; adenosine: 1 M; UPy-linker: 7.5 wt%; LAP: 0.30 wt%. This solution (1 mL) was added in a continuous organic phase of 10% ABIL EM-90 surfactant in mineral oil (20 mL) under constant agitation of ~100 rpm. The microdroplets were exposed to UV irradiation (365 nm) for 20 min to obtain microgels. The gel particles were then washed in a series of hexane, isopropanol, deionized water, and freeze-dried. Microgels without 3-APBA were synthesized similarly using acrylamide (1 M) and used as controls.

### Characterization of microgels

The size of the microgels was determined by optical microscopy. Microgels were suspended in DI water, allowed to hydrate for 24 h, and imaged using the Axio Vert.A1 microscope. ImageJ was used to determine the average diameter. The stability of the microgels was also determined by optical microscopy. Briefly, microgels (~5 mg) were suspended in DI water or growth medium (containing α-MEM, FBS (10%, v/v)) for 28 days. At predetermined timepoints, microgel samples were removed and imaged using the Axio Vert.A1 microscope. The images were then quantified using ImageJ to determine the average diameter.

**Adenosine content within the microgels.** The adenosine loading capacity was measured using UV/vis spectroscopy. A standard curve was created by using a range (4–125 µg/mL) of known adenosine concentrations in 0.1 M acetate buffer of pH 3.5. Adenosine loaded microgels (~5 mg) were suspended in 1 mL of 0.1 M acetate buffer (pH 3.5). The samples were then placed at 37 °C for 24 h and centrifuged at 6000 × g for 10 min. The supernatant was collected and measured by using UV/vis spectroscopy at 260 nm.

**Adenosine release kinetics.** The adenosine-loaded microgels (~5 mg) were hydrated in 1 mL of PBS buffer (0.1 M, pH 7.4), a 3D microgel scaffold was allowed to form and placed at 37 °C. At predetermined time points, 20% of the supernatant liquid was collected and replaced with fresh buffer. UV/vis spectroscopy was then used to determine the amount of adenosine released from the scaffolds. The free adenosine content in the buffer was quantified as a function of time, measured via UV/vis spectroscopy at 260 nm. The standard curve created using known concentrations of adenosine (4–125 µg/mL) in 0.1 M PBS buffer of pH 7.4 was used to determine the unknown concentration of adenosine in the solution.

### Rheological characterization of the microgel-based scaffolds

The HA-MA-PBA microgels were prepared in PBS (pH 7.4) and tested with a rotational rheometer (AR-G2, TA Instruments). A parallel plate geometry was used to test both samples (8 mm). Frequency sweep measurements were carried out from 0.1 to 10 Hz at a strain amplitude of 1%, and all measurements were carried out in triplicates. To evaluate the microgel network's

ability to self-heal (or regenerate following rupture), step-strain measurements were recorded at 1 Hz with 6 cycles of 1% and 500% strain, with each strain being applied for 180 s.

### Tibial fracture and microgel scaffold implantation

Mice were anesthetized with 2% isoflurane and administered with sustained release buprenorphine (1 mg/kg, ZooPharm) via subcutaneous injection before beginning surgery. First the skin proximal to the knee was removed and the knee joint exposed. The right tibia was then stabilized through insertion of a 0.7 mm pin from the tibial plateau through the medullary cavity. Following stabilization, a fracture was created at the midshaft of the tibia with blunt scissors. Finally, 30 µL of a 7.5 wt% microgel system was injected around the fracture site. Following administration, the wound was closed with wound clips and two drops of bupivacaine (0.5%, Hospira) were applied topically along the incision line.

### Microgel retention in vivo

In total, 30 µL of Cy7-containing microgels (7.5 wt%) was administered at the murine tibial fracture site *via* injection. At designated timepoints following administration, the mice were anesthetized with isoflurane and imaged *via* an IVIS Kinetic system (excitation filter, 745 nm; emission filter, ICG; excitation time, 100 ms). The Cy7 epi-fluorescence intensity at the fracture site was quantified from images taken at Day 0 and designated as the starting value. The percent of remaining fluorescence intensity at each subsequent time point was determined up to a 28-day post microgel administration, where the animals were euthanized.

### Microcomputed tomography (µCT)

The fractured tibiae were collected, and pins removed. The samples were fixed in 4% paraformaldehyde (PFA) for 1 day at 4 °C. Following fixation, the samples were rinsed with PBS and loaded into a µCT scanner (vivaCT 80, Scanco Medical) along with phantom. The samples and phantom were scanned at 55 keV with a pixel resolution of 10.4 µm. The scanned images were reconstructed using the µCT Evaluation Program V6.6 (Scanco Medical). Radiographs and 3D images were generated using µCT Ray V4.0 (Scanco Medical). Total callus volume (TV), bone mineral density (BMD), and bone volume (BV) ratio (BV/TV) was calculated using the phantom as a reference from 100 contiguous slices. Cortical alignment was determined by measuring the distance remaining between cortices at 28D post-fracture of the 3D rendered images using ImageJ (*n* = 6–7 per group).

### Histological staining

Tibial fracture samples were fixed using 4% paraformaldehyde (PFA) at 4 °C for 24 h and decalcified using 14% ethylenediaminetetraacetic acid (EDTA, pH 7.4) for 2 weeks at 4 °C. The samples were gradually dehydrated using various concentrations of ethanol and incubated in Citrisolv (Decon Laboratories, 125160) until equilibrated. Following dehydration, samples were submerged in a mixture of 50% (v/v) Citrisolv and 50% (w/w) paraffin (General Data Healthcare, H-PF) for 30 min at 70 °C. These samples were embedded in paraffin and sectioned at 5 µm with a rotary microtome (Leica, RM2255). Prior to staining, sections were deparaffinized. To visualize the extent of fracture healing, the sections were stained with either Safranin-O (Saf-O) or Movat's Pentachrome stain. For Movat's Pentachrome stain, samples were stained with Movat Pentachrome Stain Kit: Modified Russel Movat (ScyTek Laboratories Inc, MPS1). Specifically, the samples were stained with Elastic Stain (30 mL 5% Hematoxolin (SkyTek HSV250); 15 mL 10% Ferric Chloride (SkyTek FCC125); 15 mL Lugol's Iodine (SyTek LIS125)) for 20 min, Alcian Blue for 25 min (SkyTek ANC125), Biebrich Scarlet-Acid Fusion (SkyTek BSU125) for 2 min, and Metanil Yellow 10 min (SkyTek MYQ125). For Saf-O staining, sections were stained for 1 h with 1% Safranin-O (Sigma-Aldrich, Cat.# S8884) and counter-stained for 1 min in 0.02% Fast Green (Sigma-Aldrich, Cat.# F7258). Sections were gradually dehydrated using various concentrations of ethanol until equilibrium was reached. Sections were mounted using Cytoseal Mountant 60 (EpreDia, 23-244257) and imaged using a Keyence BZ-X700 microscope.

ImageJ) was used for quantification of histological images: Safranin-O staining was quantified by percentage of positive staining within the callus area; Endomucin staining was quantified by measuring the intensity of positive staining within the callus area.

### Preparation of cell suspensions and cell sorting for scRNAseq

To obtain single-cell suspensions from calluses of tibiae, mice were euthanized, and calluses were minced using a scalpel in 100 U ml<sup>-1</sup> DNase I (Millipore Sigma, 10104159001), 1% bovine serum albumin (Sigma-Aldrich) and PBS for 20 min at 37 °C. The cell suspension was filtered using a 40 µm strainers and centrifuged at 300 × g for 5 min and treated with RBC lysis buffer (Millipore Sigma, 11814389001) for 10 min. Cells were stained with propidium iodide and viable cells were sorted using DiVa cell sorter (BD Biosciences) for scRNA-seq preparation. Cell suspensions were loaded onto a 10x Genomics Chromium Controller Single-Cell Instrument (10x Genomics) mixed with reverse transcription (RT) reagents, gel beads, and oil to generate single-cell gel bead-in emulsions (GEMs). GEM-RT was performed using an Eppendorf Mastercycler Pro using the following cycle: 53 °C for 45 min, 85 °C for 5 min. After RT, GEMs were broken, and the single-strand cDNA was purified using DynaBeads MyOne Silane Beads (Thermo Fisher Scientific). cDNA was then amplified using the Eppendorf Mastercycler Pro using the following cycle: 98 °C for 3 min, 11–13 cycles of 98 °C for 15 s, 67 °C for 20 s and 72 °C for 1 min, 72 °C for 1 min. The amplified cDNA product was further purified using the SPRIselect Reagent Kit (0.6 × SPRI; Beckman Coulter). Indexed sequencing libraries were constructed using the reagents in the Chromium Single-Cell Library Kit 3' v2 using the following steps: (1) fragmentation, end repair and A-tailing, (2) SPRIselect cleanup, (3) adapter ligation, (4) post-ligation cleanup with SPRIselect, (5) sample index PCR, and (6) post-index PCR cleanup. Sequencing libraries were transferred to BGI and were loaded onto a MGISEQ-2000 platform (MGI Tech) for sequencing.

### scRNA-seq data analysis

10X Genomics reads were converted to FASTQ files using bcl2fastq command-line tool. FASTQ files were aligned to the mm10 reference transcriptome, filtered, and counted using the Cell Ranger 7.0.0 pipeline. Matrix files were used to construct Seurat (version 4.3.0) objects in R statistical software (version 4.1.3). Seurat objects were filtered and normalized on a per-sample basis to remove cells with exceedingly high or low UMIs and high mitochondrial gene expression. Unbiased clustering, marker gene identification and differential gene expression testing were all performed in Seurat. Cell type labels were generated through alignment with the ImmGen database<sup>66</sup>. After filtering, all samples were integrated into a single Seurat object using the SCTransform integration workflow. FindConservedMarkers function was used to identify cluster marker genes. FindMarkers was used to identify differentially expressed genes between control and adenosine-treated calluses. Full and split-group UMAPs were generated with Seurat's DimPlot function. UMAPs including gene expression were generated with Seurat's FeaturePlot function and the heatmap was generated using Seurat's DoHeatmap function. For RNA Velocity: Loom files were generated on a per-sample basis from the original BAM files output from the Cell Ranger pipeline using the command-line tool, Velocity (version 0.17.17). An H5AD file was exported from Seurat and imported into python for downstream analysis. Loom file data was merged with the Seurat H5AD data to form a complete annotated data set of the single-cell sequencing experiment. Using scvelo (version 0.2.5), velocities were computed through the stochastic solver and plots created using scvelo's plotting functions scvelo.pl.velocity\_embedding\_grid and scvelo.pl.scatter. For granulocyte analysis, the annotated data set was subset to include only the granulocyte clusters identified from unbiased clustering in Seurat (see scRNA-seq data analysis). Velocities and differential velocities were calculated using scvelo.tl.velocity\_graph and scvelo.tl.rank\_velocity\_genes for each granulocyte cluster. The rank\_velocity\_genes function utilizes a pre-computed velocity graph and performs Welch's t-test with an overestimated variance on the velocity expression. Consequently, for each gene, the

dynamics (i.e., velocity vector) of that gene is compared between clusters using the *t* test.

### Statistical analyses

All numerical data are expressed as means plus or minus standard error of the mean. Data were subjected to one-way analysis of variance (ANOVA with post hoc Tukey-Kramer test for multiple comparisons), or two-tailed Student's *t*-test. *P*-values of less than 0.05 were considered statistically significant and indicated with an asterisk. All statistical analyses were performed with GraphPad Prism 9.1.0.

### Data availability

Further information and requests for resources and reagents should be directed to and will be provided by the lead contact, S.V. (shyni.varghese@duke.edu). RNA-sequencing data generated in this study has been deposited at The Gene Expression Omnibus (GEO) database, supported by the National Center for Biotechnology Information (NCBI), and are publicly available as of the date of publication (Accession Number: GSE272155). Any additional information required to reanalyze the data reported in this paper is available by the lead contact upon request.

### Code availability

This paper does not report original code.

Received: 12 July 2024; Accepted: 27 March 2025;

Published online: 09 April 2025

### References

- Meinberg, E. G., Clark, D., Miclau, K. R., Marcucio, R. & Miclau, T. Fracture repair in the elderly: Clinical and experimental considerations. *Injury* **50**, S62–s65 (2019).
- Foulke, B. A., Kendal, A. R., Murray, D. W. & Pandit, H. Fracture healing in the elderly: A review. *Maturitas* **92**, 49–55 (2016).
- Clark, D., Nakamura, M., Miclau, T. & Marcucio, R. Effects of aging on fracture healing. *Curr. Osteoporos. Rep.* **15**, 601–608 (2017).
- Arinzon, Z., Fidelman, Z., Zuta, A., Peisakh, A. & Berner, Y. N. Functional recovery after hip fracture in old-old elderly patients. *Arch. Gerontol. Geriatr.* **40**, 327–336 (2005).
- Tang, V. L. et al. Rates of recovery to pre-fracture function in older persons with hip fracture: An Observational Study. *J. Gen. Intern. Med.* **32**, 153–158 (2017).
- Chou, S.-E. et al. Risk factors and complications contributing to mortality in elderly patients with fall-induced femoral fracture: A cross-sectional analysis based on trauma registry data of 2,407 patients. *Int. J. Surg.* **66**, 48–52 (2019).
- Morri, M. et al. One-year mortality after hip fracture surgery and prognostic factors: a prospective cohort study. *Sci. Rep.* **9**, 18718 (2019).
- Burge, R. et al. Incidence and Economic Burden of Osteoporosis-Related Fractures in the United States, 2005–2025. *J. Bone Miner. Res.* **22**, 465–475 (2007).
- Migliorini, F. et al. Fragility fractures: Risk factors and management in the elderly. *Med. (Kaunas)* **57**, 1119 (2021).
- Bledsoe, L., Alessi, K., Toro, J. B., Giordano, B. & Hanypsiak, B. T. Fragility fractures: diagnosis and treatment. *Am. J. Orthop. (Belle Mead NJ)* **47** (2018).
- Duan, X., Al-Qwbani, M., Zeng, Y., Zhang, W. & Xiang, Z. Intramedullary nailing for tibial shaft fractures in adults. *Cochrane Database Syst. Rev.* **1**, CD008241 (2012).
- Gosler, M. W., Testroote, M., Morrenhof, J. W. & Janzing, H. M. Surgical versus non-surgical interventions for treating humeral shaft fractures in adults. *Cochrane Database Syst. Rev.* **1**, CD008832 (2012).
- Chang, A. K., Bijur, P. E., Esses, D., Barnaby, D. P. & Baer, J. Effect of a single dose of oral opioid and nonopioid analgesics on acute

- extremity pain in the emergency department: A randomized clinical trial. *JAMA* **318**, 1661–1667 (2017).
14. Hak, D. J. et al. Delayed union and nonunions: Epidemiology, clinical issues, and financial aspects. *Injury* **45**, S3–S7 (2014).
  15. Holmes, D. Non-union bone fracture: a quicker fix. *Nature* **550**, S193 (2017).
  16. Zura, R. et al. Epidemiology of fracture nonunion in 18 human bones. *JAMA Surg.* **151**, e162775 (2016).
  17. Josephson, A. M. et al. Age-related inflammation triggers skeletal stem/progenitor cell dysfunction. *Proc. Natl. Acad. Sci. USA* **116**, 6995–7004 (2019).
  18. Grosso, A. et al. It takes two to tango: Coupling of angiogenesis and osteogenesis for bone regeneration. *Front Bioeng. Biotechnol.* **5**, 68 (2017).
  19. Vi, L. et al. Macrophage cells secrete factors including LRP1 that orchestrate the rejuvenation of bone repair in mice. *Nat. Commun.* **9**, 5191 (2018).
  20. Virk, M. S. & Lieberman, J. R. Biologic adjuvants for fracture healing. *Arthritis Res Ther.* **14**, 225–225 (2012).
  21. Marmor, M. T., Matz, J., McClellan, R. T., Medam, R. & Miclau, T. Use of osteobiologics for fracture management: The when, what, and how. *Injury* **52**, S35–S43 (2021).
  22. Roberts, S. J. & Ke, H. Z. Anabolic strategies to augment bone fracture healing. *Curr. Osteoporos. Rep.* **16**, 289–298 (2018).
  23. Bennett, P. M., Stewart, S. K., Dretzke, J., Bem, D. & Penn-Barwell, J. G. Preclinical therapies to prevent or treat fracture non-union: A systematic review. *PLoS One* **13**, e0201077 (2018).
  24. Vantucci, C. E. et al. BMP-2 delivery strategy modulates local bone regeneration and systemic immune responses to complex extremity trauma. *Biomater. Sci.* **9**, 1668–1682 (2021).
  25. Subbiah, R. et al. Triple growth factor delivery promotes functional bone regeneration following composite musculoskeletal trauma. *Acta Biomater.* **127**, 180–192 (2021).
  26. Wu, S. et al. Rat bone marrow mesenchymal stem cells induced by rPDGF-BB promotes bone regeneration during distraction osteogenesis. *Front Bioeng. Biotechnol.* **11**, 1110703 (2023).
  27. Zeng, Y., Hoque, J. & Varghese, S. Biomaterial-assisted local and systemic delivery of bioactive agents for bone repair. *Acta Biomater.* **93**, 152–168 (2019).
  28. Carroll, S. H. et al. A2B adenosine receptor promotes mesenchymal stem cell differentiation to osteoblasts and bone formation in vivo. *J. Biol. Chem.* **287**, 15718–15727 (2012).
  29. Mediero, A., Kara, F. M., Wilder, T. & Cronstein, B. N. Adenosine A(2A) receptor ligation inhibits osteoclast formation. *Am. J. Pathol.* **180**, 775–786 (2012).
  30. Auchampach, J. A. Adenosine receptors and angiogenesis. *Circ. Res* **101**, 1075–1077 (2007).
  31. Kang, H., Shih, Y. R. & Varghese, S. Biomaterialized matrices dominate soluble cues to direct osteogenic differentiation of human mesenchymal stem cells through adenosine signaling. *Biomacromolecules* **16**, 1050–1061 (2015).
  32. Shih, Y. R. et al. Calcium phosphate-bearing matrices induce osteogenic differentiation of stem cells through adenosine signaling. *Proc. Natl. Acad. Sci. USA* **111**, 990–995 (2014).
  33. Takedachi, M. et al. CD73-generated adenosine promotes osteoblast differentiation. *J. Cell Physiol.* **227**, 2622–2631 (2012).
  34. Jacobson, K. A. & Gao, Z. G. Adenosine receptors as therapeutic targets. *Nat. Rev. Drug Discov.* **5**, 247–264 (2006).
  35. Borea, P. A., Gessi, S., Merighi, S., Vincenzi, F. & Varani, K. Pharmacology of Adenosine Receptors: The State of the Art. *Physiol. Rev.* **98**, 1591–1625 (2018).
  36. Cronstein, B. N. & Sitkovsky, M. Adenosine and adenosine receptors in the pathogenesis and treatment of rheumatic diseases. *Nat. Rev. Rheumatol.* **13**, 41–51 (2017).
  37. Bradaschia-Correa, V. et al. Ecto-5'-nucleotidase (CD73) regulates bone formation and remodeling during intramembranous bone repair in aging mice. *Tissue Cell* **49**, 545–551 (2017).
  38. Mediero, A., Wilder, T., Perez-Aso, M. & Cronstein, B. N. Direct or indirect stimulation of adenosine A2A receptors enhances bone regeneration as well as bone morphogenetic protein-2. *FASEB J.* **29**, 1577–1590 (2015).
  39. Bogan, K. L. & Brenner, C. 5'-Nucleotidases and their new roles in NAD<sup>+</sup> and phosphate metabolism. *N. J. Chem.* **34**, 845–853 (2010).
  40. Newman, H. & Varghese, S. Extracellular adenosine signaling in bone health and disease. *Curr. Opin. Pharm.* **70**, 102378 (2023).
  41. Shih, Y. V. et al. Dysregulation of ectonucleotidase-mediated extracellular adenosine during postmenopausal bone loss. *Sci. Adv.* **5**, eaax1387 (2019).
  42. Colgan, S. P., Eltzschig, H. K., Eckle, T. & Thompson, L. F. Physiological roles for ecto-5'-nucleotidase (CD73). *Purinergic Signal* **2**, 351–360 (2006).
  43. Hoque, J. et al. Microgel-assisted delivery of adenosine to accelerate fracture healing. *ACS Biomater. Sci. Eng.* **8**, 4863–4872 (2022).
  44. Zeng, Y., Shih, Y.-R. V., Baht, G. S. & Varghese, S. In vivo sequestration of innate small molecules to promote bone healing. *Adv. Mater.* **32**, 1906022 (2020).
  45. Gilpin, A. et al. Self-healing of hyaluronic acid to improve in vivo retention and function. *Adv. Healthc. Mater.* **10**, 2100777 (2021).
  46. Lybrand, K., Bragdon, B. & Gerstenfeld, L. Mouse models of bone healing: fracture, marrow ablation, and distraction osteogenesis. *Curr. Protoc. Mouse Biol.* **5**, 35–49 (2015).
  47. Street, J. et al. Vascular endothelial growth factor stimulates bone repair by promoting angiogenesis and bone turnover. *Proc. Natl. Acad. Sci. USA* **99**, 9656–9661 (2002).
  48. Graham, S. et al. Investigating the role of PDGF as a potential drug therapy in bone formation and fracture healing. *Expert Opin. Investig. Drugs* **18**, 1633–1654 (2009).
  49. Schmidmaier, G. et al. Improvement of fracture healing by systemic administration of growth hormone and local application of insulin-like growth factor-1 and transforming growth factor-beta1. *Bone* **31**, 165–172 (2002).
  50. Newman, H., Shih, Y. V. & Varghese, S. Resolution of inflammation in bone regeneration: From understandings to therapeutic applications. *Biomaterials* **277**, 121114 (2021).
  51. La Manno, G. et al. RNA velocity of single cells. *Nature* **560**, 494–498 (2018).
  52. Lu, C. et al. Effect of age on vascularization during fracture repair. *J. Orthop. Res* **26**, 1384–1389 (2008).
  53. Sethe, S., Scutt, A. & Stolzing, A. Aging of mesenchymal stem cells. *Ageing Res Rev.* **5**, 91–116 (2006).
  54. Bobby Gaspar, H. Bone marrow transplantation and alternatives for adenosine deaminase deficiency. *Immunol. Allergy Clin. North Am.* **30**, 221–236 (2010).
  55. van der Hoeven, D., Wan, T. C. & Auchampach, J. A. Activation of the A(3) adenosine receptor suppresses superoxide production and chemotaxis of mouse bone marrow neutrophils. *Mol. Pharm.* **74**, 685–696 (2008).
  56. Salvatore, C. A. et al. Disruption of the A(3) adenosine receptor gene in mice and its effect on stimulated inflammatory cells. *J. Biol. Chem.* **275**, 4429–4434 (2000).
  57. Jacobson, K. A. et al. A3 adenosine receptors as modulators of inflammation: From medicinal chemistry to therapy. *Med. Res. Rev.* **38**, 1031–1072 (2018).
  58. Ren, T. H., Lv, M. M., An, X. M., Leung, W. K. & Seto, W.-K. Activation of adenosine A3 receptor inhibits inflammatory cytokine production in colonic mucosa of patients with ulcerative colitis by down-regulating the nuclear factor-kappa B signaling. *J. Digest. Dis.* **21**, 38–45 (2020).

59. Cohen, S. & Fishman, P. Targeting the A(3) adenosine receptor to treat cytokine release syndrome in cancer immunotherapy. *Drug Des. Devel Ther.* **13**, 491–497 (2019).
60. Sipka, S. et al. Adenosine inhibits the release of interleukin-1 $\beta$  in activated human peripheral mononuclear cells. *Cytokine* **31**, 258–263 (2005).
61. Farr, S. A. et al. Adenosine A3 receptor as a novel therapeutic target to reduce secondary events and improve neurocognitive functions following traumatic brain injury. *J. Neuroinflamm.* **17**, 339 (2020).
62. Ernens, I. et al. Adenosine up-regulates vascular endothelial growth factor in human macrophages. *Biochem Biophys. Res Commun.* **392**, 351–356 (2010).
63. Kostenuik, P. & Mirza, F. M. Fracture healing physiology and the quest for therapies for delayed healing and nonunion. *J. Orthop. Res.* **35**, 213–223 (2017).
64. Ma, C. et al. Exogenous PTH 1-34 attenuates impaired fracture healing in endogenous PTH deficiency mice via activating indian Hedgehog signaling pathway and accelerating endochondral ossification. *Front Cell Dev. Biol.* **9**, 750878 (2021).
65. Hoque, J. et al. Bone targeting nanocarrier-assisted delivery of adenosine to combat osteoporotic bone loss. *Biomaterials* **273**, 120819 (2021).
66. Heng, T. S., Painter, M. W. & Immunological Genome Project, C. The Immunological Genome Project: Networks of gene expression in immune cells. *Nat. Immunol.* **9**, 1091–1094 (2008).
- B.A.A. supervised this study. S.V. conceptualized and supervised this study, provided funding, interpreted data, and wrote and revised the manuscript.

### Competing interests

Authors H.N. and S.V. are co-founders of OsteoCure Therapeutics, but and declare no non-financial competing interests. All other authors declare no financial or non-financial competing interests.

### Additional information

**Supplementary information** The online version contains supplementary material available at <https://doi.org/10.1038/s41536-025-00406-1>.

**Correspondence** and requests for materials should be addressed to Shyni Varghese.

**Reprints and permissions information** is available at <http://www.nature.com/reprints>

**Publisher's note** Springer Nature remains neutral with regard to jurisdictional claims in published maps and institutional affiliations.

**Open Access** This article is licensed under a Creative Commons Attribution-NonCommercial-NoDerivatives 4.0 International License, which permits any non-commercial use, sharing, distribution and reproduction in any medium or format, as long as you give appropriate credit to the original author(s) and the source, provide a link to the Creative Commons licence, and indicate if you modified the licensed material. You do not have permission under this licence to share adapted material derived from this article or parts of it. The images or other third party material in this article are included in the article's Creative Commons licence, unless indicated otherwise in a credit line to the material. If material is not included in the article's Creative Commons licence and your intended use is not permitted by statutory regulation or exceeds the permitted use, you will need to obtain permission directly from the copyright holder. To view a copy of this licence, visit <http://creativecommons.org/licenses/by-nc-nd/4.0/>.

© The Author(s) 2025

### Acknowledgements

We acknowledge the financial support from National Institute on Aging of the National Institutes of Health (NIH) under Award Number R01 AG 074491.

### Author contributions

H.N. conceptualized this study, designed and performed experiments, analyzed data, and wrote and revised the manuscript. Y.R.V.S. performed experiments, analyzed data, and revised the manuscript. J.H. performed experiments, analyzed data, and revised the manuscript. Y.Z. performed experiments and analyzed data. N.R.N. performed experiments, analyzed data, and revised the manuscript. G.G. performed experiments, analyzed data, and revised the manuscript. W.G. performed experiments and analyzed data. V.P. performed experiments. C.W. supervised this study.